ARTICLE OPEN

Theory of non-Hermitian topological whispering gallery

René Pernas-Salomón [ID][1 ✉], Li-Yang Zheng[2], Zhiwang Zhang [ID][3], Penglin Gao[4,5], Xiaojun Liu[3], Ying Cheng[3 ✉] and Johan Christensen [ID][1,6 ✉]

Topological insulators have taken the condensed matter physics scenery by storm and captivated the interest among scientists and materials engineers alike. Surprisingly, this arena which was initially established and profoundly studied in electronic systems and crystals, has sparked a drive among classical physicists to pursue a wave-based analogy for sound, light and vibrations. In the latest efforts combining valley-contrasting topological sound with non-Hermitian ingredients, B. Hu et al. [Nature **597**, 655 (2021)] employed thermoacoustic coupling in sonic lattices whose elementary building blocks are coated with electrically biased carbon nanotube films. In this contribution, we take a theoretical and numerical route towards understanding the complex acoustic interplay between geometry and added acoustic gain as inspired by the aforesaid publication. Besides complex bulk and edge states predictions and computations of mode-split resonances using whispering gallery configurations, we also predict an acoustic amplitude saturation in dependence on the activated coated elements. We foresee that our computational advances may assist future efforts in exploring thermoacoustic topological properties.

INTRODUCTION

A laser, as the acronym implies, produces amplified and coherent light through stimulated emission of radiation. These devices are found in countless applications, ranging from bar-code scanners, laser printers, DVD players, etc., but are also commonly used in industry, communications, and medicine. In those devices, optical amplification takes place when photons undergo stimulated emission of excited atoms, which happens when a population inversion is present. For this to take place, however, an optical gain medium is inevitable. But for the case of sound, at audible kHz and ultrasonic MHz frequencies, which is where classical vibrations persist, no such analogy exist. Equivalent "sasers" would have the groundbreaking potential to revolutionize sound-based imaging and detection, but would possibly also push forward new paradigms in communications. For contemporary studies in non-Hermitian topology when sound waves are considered, artificial lattices executing acoustic amplification would require an analogue acoustic gain medium.

Valley-Hall effects reside at the frontier in a very active arena of condensed matter physics, where associated valley-Hall topological insulators are considered as a particularly popular member among exotic structures, capable to confine states thanks to their underlying topology[1–3]. Steadfast valley transport requires no breaking of the time-reversal symmetry, but remains resilient only under certain symmetry-preserving defects or imperfections. The topology is usually defined across the entire band within the Brillouin zone (BZ), however, concerning valley-contrasting physics, a non-zero topological charge called the valley Chern number, is found to be localized around the valleys at the corners of the BZ. The valleys, i.e., the band extrema of the gapped Dirac cones, are formed by lifting the inversion symmetry of the lattice and carry opposite topological charges, which implies that their corresponding vortex states have differing chirality that can be

harnessed to launch one-way valley transport, beam splitting and refraction control of out-coupled valley edge excitations[4–11].

Expanding on exclusive non-Hermitian topological phases by adding gain or loss channels, marks the latest frontier in this flourishing field, which now also entails complex topology[12–21]. The bulk-edge correspondence conventionally establishes a bridge between the Bloch band topology and topological edge states. However, the combination of non-Hermitian and topological components, broadens the horizon of phase transitions that strongly challenge the bulk-edge correspondence by breaking with its most common conventions. A colorful example along this line, is the so-called non-Hermitian skin effect[22–28], a phenomenon that features an abnormal localization of bulk states. Based on on-site dissipations or nonreciprocal coupling among artificial atoms, i.e., cavities, waveguides, fibers, etc., translational symmetry breaking is induced in finite configurations and responsible for the inadequacy of conventional Bloch band descriptions[29–31].

In this work, we study valley-Hall inspired topology in an equivalent acoustic setting. Inspired by the experimental study by Hu et al.[32] we conduct numerical computations of the sonic lattice whose thermoplastic [acrylonitrile butadiene styrene (ABS)] rods are coated by carbon nanotube (CNT) films, which, when activated, generate the desired non-Hermitian acoustic contribution. Our computations that are based on plane wave expansions display remarkable agreement to finite element simulations, both for the bulk and the projected surface dispersion relation. Moreover, by using a multiple scattering approach, we are able to reconstruct numerically the complex acoustic signatures of the fabricated triangular topological whispering gallery sonic crystal. In a relatively narrow topological band gap, we discuss the whispering gallery mode-split amplitudes obtained by different techniques. Lastly, our numerical predictions also confirm how the average mode-split amplitude exhibits acoustic gain saturation in dependence with the number of activated rows involved in the

[1]Department of Physics, Universidad Carlos III de Madrid, Madrid, Spain. [2]School of Science, Shenzhen Campus of Sun Yat-sen University, Shenzhen 518107, China. [3]Department of Physics, MOE Key Laboratory of Modern Acoustics, Collaborative Innovation Center of Advanced Microstructures, Nanjing University, Nanjing, China. [4]State Key Laboratory of Mechanical System and Vibration, Shanghai Jiao Tong University, Shanghai 200240, China. [5]Institute of Vibration, Shock and Noise, Shanghai Jiao Tong University, Shanghai 200240, China. [6]IMDEA Materials Institute, Calle Eric Kandel, 2, 28906 Getafe, Madrid, Spain. ✉email: rpernas@fis.uc3m.es; chengying@nju.edu.cn; johan.christensen@imdea.org
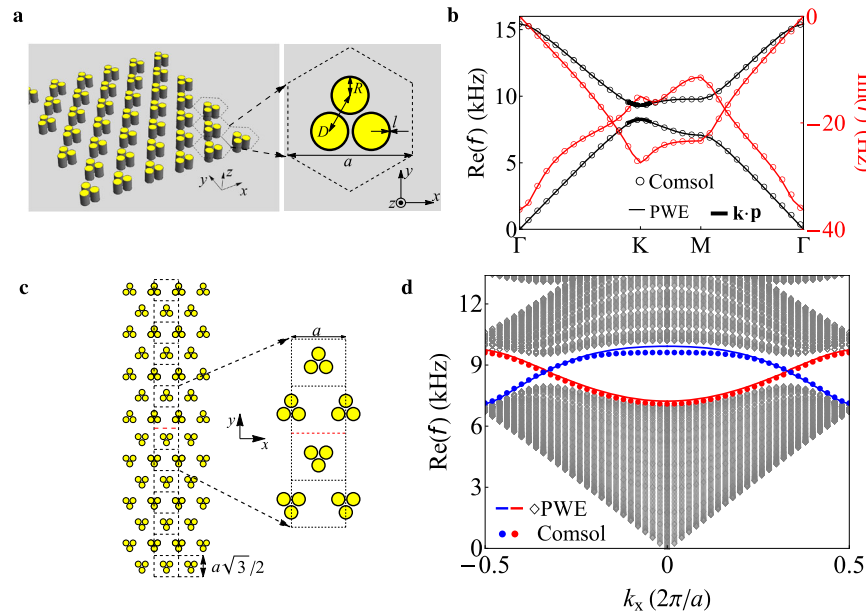
Fig. 1 Band structure of the non-Hermitian sonic kagome lattice. a Illustration of the non-Hermitian lattice under investigation, including a magnification of the unit cell whose rigid cylinders are coated by a complex fluid-layer of thickness $l = 0.1R$ to emulate the activated CNT film. **b** With a non-Hermiticity factor $\beta = 0.05$ of the complex mass density, the real (imaginary) dispersion bands are shown on the left (right) axis as obtained through the PWE method, finite element simulations (COMSOL) and a $\mathbf{k} \cdot \mathbf{p}$ method (only around the K-point). **c** Schematic of the sonic valley-Hall zig-zag interface (red dashed line) whose supercell of size $a \times 7a\sqrt{3}$ is highlighted by the black dashed line. The inset provides a clearer view of the rigid cylinders involved in the rectangular supercell structure. **d** Real valley-edge dispersion for the non-Hermitian supercell shown in **c**. The gray diamonds and the colored (red and blue) solid lines represent the bulk and the valley-projected edge states, respectively, using the PWE method. The corresponding colored dots represent the edge sates obtained by Finite-element simulations.

lattice. Our work highlights, on a numerical level, the scattering mechanisms leading to topological mode splitting of whispering gallery resonances in the presence of thermoacoustic gain, which are promising for applications related to acoustic communication and sensing.

RESULTS

Topological modes in a non-Hermitian lattice

The topological whispering-gallery (WG) insulator devised by Hu et al.[32] consists of a triangular sonic crystal made of ABS rods, each coated by CNT films whose ends are connected to a time-varying electric current. Figure 1a displays the so-called kagome lattice used in the experiments, which in fact is a triangular Bravais lattice. Upon closer inspection of the inset in Fig. 1a, one can discern the coating region of thickness l. This non-Hermitian lattice is being treated as a fluid-acoustic periodic system, hence, the modeling will be based on a linear inhomogeneous acoustic wave equation

$$\frac{1}{B(\mathbf{r})} \frac{\partial^2 P(\mathbf{r}, t)}{\partial t^2} = \nabla \cdot \left(\frac{\nabla P(\mathbf{r}, t)}{\rho(\mathbf{r})} \right), \tag{1}$$

where P is the pressure, while ρ and B represent the mass density and the bulk modulus respectively. To simplify the analysis, we treat the ABS rods as perfect rigid bodies, whereas the CNT film coatings are modeled as complex fluid layers comprising a complex mass density $\rho_{CNT} = \rho_0(1 + i\beta)$, where ρ_0 corresponds to the mass density of air and β represents its non-Hermitian component that accounts for wave amplification. As we detail in the "Method" section, by using a Plane Wave Expansion (PWE) approach, the inhomogeneous wave equation in Eq. (1) can be rewritten into a generalized eigenvalue problem to compute the complex band diagram shown in Fig. 1b. Moreover, as additionally detailed in the Method section, we also employ a $\mathbf{k} \cdot \mathbf{p}$ method that is a semi-empirical approach to calculate the electronic band

structure, however, it has lately been used in classical photonic and phononic settings as well[33]. In particular, the analytical $\mathbf{k} \cdot \mathbf{p}$ method is only used to compute the real bands around the K-point, yet, both methods compared to finite element simulations, display a well agreeing gapped Dirac dispersion. Moreover, the negative imaginary axis, showcases how the two bands exhibit wave amplification.

The PWE method can be easily extended (see method) for larger supercells as is necessary when computing the valley-polarized edge dispersion diagram. In order to do so, we design a rectangular supercell as shown in Fig. 1c. This thin strip is composed of two adjacently facing (red dashed line) sonic lattices of opposite valley phases. Interestingly, along the y-axis, with the lattice constant of $a\sqrt{3}/2$, consecutive cells host alternating complete and incomplete trimers. Since the supercell is Bloch-periodic in all direction, with one single supercell computation, we obtain two edge-dispersion bands (blue and red) inside the gap of the projected bulk bands (gray diamonds) as shown in Fig. 1d. The periodicity invoked at the upper and lower strip terminations, incidentally produces multiple valley-Hall zig-zag interfaces, yet they vary between back-to-back and tip-to-tip (of the trimers) contacts. In other words, in one single computation we obtain the edge dispersion of both the negative and positive-type inter-face[34]. Indeed, these two edge-dispersion bands as shown in Fig. 1d, are in good agreement with COMSOL simulations.

Whispering-gallery mode splitting

Before we begin to model the actual non-Hermitian topological WG resonator, we take a close look at the unit cell comprising the trimers made of CNT-coated rigid rods. Earlier, in the PWE method, we modeled those elements by means of perfectly rigid cylinders that are coated by a complex fluid layer. In what follows, using the multiple scattering theory (MST), we take a different route in analyzing the scattering characteristics of finite structures with engineered broken chirality. As shown in the inset of Fig. 2a, we
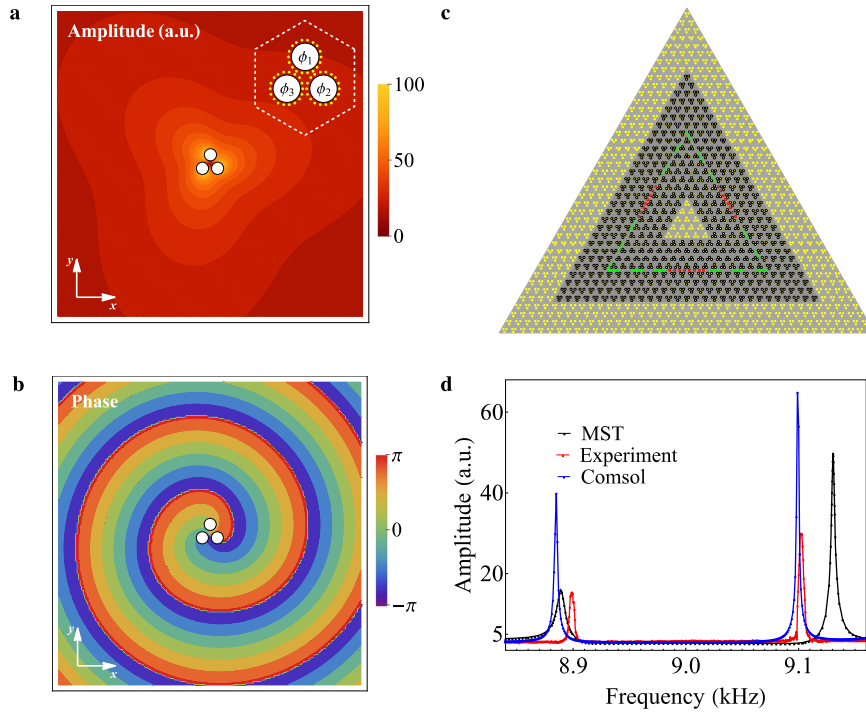
Fig. 2 Chiral whispering-gallery modes. a, b Characterising the near- and far-field emission features of isolated trimers by means of uniformly distributed point sources surrounding each rod using the MST (see inset). In here, the emission phases are set to $\phi_1 = 0$, $\phi_2 = 2\pi/3$ and $\phi_3 = -2\pi/3$, resulting in a full gain cycle of $\phi = 2\pi$. The anisotropic pressure field is accompanied by a left-handed chiral phase profile. **c** A triangular WG interface (green dashed line) is created that separates two sonic crystals of opposite topological phase. The shaded area marks the zone inside which the cylinders are coated by the activated CNT layers. The red dots indicate the equidistant points from where the average pressure amplitudes have been evaluated. **d** Chiral WG amplitude spectrum (of order $m = 27$), obtained from numerical and experimental[32] evaluations for a gain-phase texture $\phi = 2\pi$.

model the active rods by uniformly distributing a number of acoustic point sources around each cylinder. These "source rings", when using the MST, emulate the activated CNT film coatings. Beyond the trimer, generally speaking, the scattering environment consists of N-cylinders located at $\mathbf{R}_a$ (with $a = 1, 2, \ldots, N$). When sound, emanating a single point source P^0, or multiple thereof, impinges the cluster of cylinders, the total pressure is given by $P = P^0 + P^{sc}$, where P^{sc} is the total scattered field from all individual a-cylinders. At a given position $\mathbf{r}$, in polar coordinates (r, θ), we have

$$P^{sc}(r, \theta) = \sum_{a=1}^{N} \sum_{q=-\infty}^{\infty} (A_a)_q H_q(k_0 r_a) e^{iq\theta_a}, \quad (2)$$

where H_q is the q-th order Hankel function of the first kind, $k_0 = \omega/c_0$ is the wavenumber and (r_a, θ_a) are the polar coordinates in the reference frame located in the center of the a-cylinders, i.e., $\mathbf{r}_a = \mathbf{r} - \mathbf{R}_a$. Since P^0 is known, $(A_a)_q$ are the coefficients to be determined (Methods). In the figure inset of Fig. 2a it is further shown that the group of source-rings each emit sound at a given phase. As detailed in the figure caption, the specific phase arrangement ensures a so-called full gain cycle of $\phi = 2\pi$, i.e., a complete control over the chiral symmetry in the ensuing problem. Yet, Fig. 2a displays the computed pressure field distribution from the isolated trimer. More importantly, its phase distribution shown in Fig. 2b exhibits an enforced left-handed phase profile.

With a total of 1176 trimers, i.e., 3528 rods, we simulate the non-Hermitian acoustic response of a triangular WG structure as shown in Fig. 2c (fewer trimers are shown here). The geometry corresponds to exactly the same configuration as implemented by Hu et al.[32]. Moreover, from this contribution, we reuse the experimental data in the analysis that follows. The dashed green line in Fig. 2c highlights the topological valley interface, while the

gray shaded zone marks the region inside which the trimers have been coated by CNT films. In the present case, four rows in either insulator section are activated. With a full left-handed gain phase texture as discussed earlier, we are able to break the chiral symmetry of the $m = 27$ WG mode that resides within the nontrivial band gap. The circumferential length of the WG defines the splitting width, however, the clockwise and counterclockwise WG modes are carried by the respective valley-polarized edge states. Thus, in Fig. 2d, we compute the pressure amplitude spectra comprising both modes by means of averaging the field at each gallery-edge (as indicated in Fig. 2c). Despite marginal variations, the amplitude spectra display good agreement among our MST, finite element simulations and experimental data. In here, clearly the mode splitting is observed, where each peak constitutes a topologically protected chiral WG edge state.

Whispering-gallery gain saturation
In the experiments, increasing the electric current through the CNT films will generate a stronger electro-thermoacoustic coupling and eventually produce enhanced mode-split pressure amplitudes.

However, in what follows, we employ our MST to seek for a gain saturation on the basis of the non-Hermitian WG lattice itself. As stated earlier, the WG waves revolve the enclosure through the valley-polarized edge-confined states. Those surface states are confined at the interface and decay exponentially at finite penetration depths, perpendicularly into the bulk of the lattice. Intuitively, it means, the approach to increase sound amplification by steadily increasing the number of rows comprising CNT-coated trimers, must cease to have an effect at a certain threshold. Thus, in the present study, into either direction across the topological interface (Fig. 2c), we successively increase the number of active
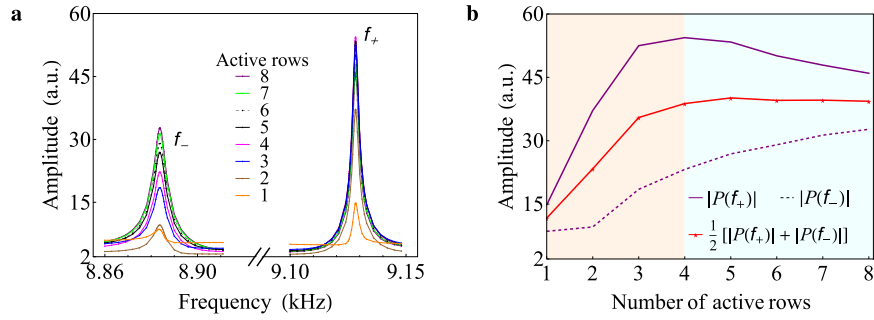
Fig. 3 Whispering gallery gain saturation. a Computed chiral WG mode spectra using the MST for an increasing number of active rows in each insulator region. The plotted range displays an activation, from 12.5% to 100%, of all involved cylinders of the WG sonic lattice. **b** The average of the two chiral WG mode-amplitudes, i.e., $|P(f_-)|$ and $|P(f_+)|$, displays gain saturation from the onset of four active row, i.e., eight total rows.

rows and conduct spectral computations of the chiral pressure amplitudes using the MST. In Fig. 3a it is clearly seen that when more active rows are involved the amplitude grows. Yet, upon closer inspection in Fig. 3b, our simulations reveal that the $|P(f_-)|$ peak steadily grows while the $|P(f_+)|$ one drops after reaching its peak. The average of the both, the red line in Fig. 3b, however, clearly marks the threshold (in this case: four active rows), beyond which additionally introduced acoustic gain fails to reach the topological interface, along which the amplitude of the WG edge states reaches saturation.

DISCUSSION

On a general note, expanding on exclusive topological phases in non-Hermitian settings using loss or gain with no Hermitian counterpart, is currently thriving. In the method section, using the $\mathbf{k} \cdot \mathbf{p}$, we argued that when using moderate gain levels ($\beta = 0.05$, in our study), the topological properties can be well characterized by a quasi-Hermitian topological valley-Chern number, since only the eigenfrequency will be affected. This also implies that the bulk-edge correspondence still applies and phenomena such as the skin effect cannot be found here. Beyond this, the precise relation between the valley-Hall effect and the non-Hermitian WG physics has several layers. For one, adding gain to our valley-Hall sonic lattices produces amplifying topological edge states.Further, the WG modes in fact are carried by these complex edge states. With an appropriate gain phase texture added to the lattice unit cell, those modes become chiral, i.e., they are mode split with the handedness according to the valley polarization. E.g., the clockwise spinning WG mode is projected from the complex K valley.

In summary, we investigated the generation of mode-split whispering gallery edge states in a topological sonic lattice executing acoustic gain. By modeling the thermoplastic rods that were decorated by carbon nanotube films through either complex fluids or so-called source-rings, we obtained good agreement with experimental and finite element data. Interestingly, when using the coated elements as the only component for controlling the acoustic gain, i.e., the non-Hermitian contribution, we found that a gain saturation sets in at the threshold of four active lattice rows into either insulator-half. This number could be further adjusted by means of engineering the geometrical scales of the topological whispering gallery insulator.

METHODS

The numerical results reported in this work were calculated using the following set of acoustic and geometrical parameters. For the background medium (air) the mass density $\rho_0 = 1.22$ kg m^{-3} and the sound speed $c_0 = 342.0$ ms^{-1}. The inset of Fig. 1a illustrates

three identical cylinders with radius $R = 0.30$ cm whose centers are placed at the vertexes of an equilateral triangle of side length $D = 0.69$ cm, and lattice constant $a = 2.17$ cm. In the inset of Fig. 2a we surround each rigid cylinder with $n_p = 18$ monopole point sources.

Plane wave expansion method

For the non-Hermitian triangular lattice depicted in Fig. 1a we choose the primitive lattice vectors $\mathbf{a}_1 = a\mathbf{x}$ and $\mathbf{a}_2 = \frac{a}{2}(\mathbf{x} + \sqrt{3}\mathbf{y})$, where a is the lattice constant and $\mathbf{x}$, $\mathbf{y}$ are the unit vectors of the lattice. Accordingly, the reciprocal lattice is built by the set of vectors $\mathbf{G} = n_1\mathbf{g}_1 + n_2\mathbf{g}_2$ where n_1, n_2 are integers and the primitive reciprocal lattice vectors $\mathbf{g}_1 = \frac{2\pi}{a}(\mathbf{x} - \mathbf{y}/\sqrt{3})$ and $\mathbf{g}_2 = (4\pi/a\sqrt{3})\mathbf{y}$. Since the Bulk modulus $B(\mathbf{r})$ and the mass density $\rho(\mathbf{r})$ are periodic in 2D, we express their reciprocal functions as Fourier series

$$\frac{1}{B(\mathbf{r})} = \sum_{\mathbf{G}} \epsilon(\mathbf{G})e^{i\mathbf{G}\cdot\mathbf{r}}, \qquad \frac{1}{\rho(\mathbf{r})} = \sum_{\mathbf{G}} v(\mathbf{G})e^{i\mathbf{G}\cdot\mathbf{r}}, \tag{3}$$

with Fourier coefficients given by integration over the unit cell

$$\epsilon(\mathbf{G}) = \frac{1}{A_{uc}} \int_S \frac{1}{B(\mathbf{r})} e^{-i\mathbf{G}\cdot\mathbf{r}} ds, \quad v(\mathbf{G}) = \frac{1}{A_{uc}} \int_S \frac{1}{\rho(\mathbf{r})} e^{-i\mathbf{G}\cdot\mathbf{r}} ds, \tag{4}$$

with the unit cell area $A_{uc} = a^2\sqrt{3}/2$. Likewise, we write the Bloch pressure

$$P(\mathbf{r}, t) = e^{i(\mathbf{k}\cdot\mathbf{r}-\omega t)} \sum_{\mathbf{G}} P_{\mathbf{k}}(\mathbf{G})e^{i\mathbf{G}\cdot\mathbf{r}}. \tag{5}$$

Substituting Eqs. (3) and (5) into Eq. (1) leads to the generalized eigenvalue problem

$$\sum_{\mathbf{G}} \left[\omega^2 \epsilon(\mathbf{G}' - \mathbf{G}) - (\mathbf{k} + \mathbf{G}) \cdot (\mathbf{k} + \mathbf{G}') v(\mathbf{G}' - \mathbf{G})\right] P_{\mathbf{k}}(\mathbf{G}) = 0. \tag{6}$$

For the j-th cylinder we consider the filling fractions $f_j = \pi R_j^2/A_{uc}$ and $f_j^{CNT} = \pi(R_j + l_j)^2/A_{uc}, j = 1, 2, 3$. We denote by $\mathbf{r}_j^0$ the position vector of the center of the j-th cylinder in the reference frame of the unit cell. To obtain the analytic expressions for the coefficients $v(\mathbf{G})$ and $\epsilon(\mathbf{G})$ we first expand the integrals in Eq. (4) over the area of the unit cell. The result can be written in the form

$$v(\mathbf{G}) = \frac{1}{A_{uc}} \left[\frac{1}{\rho_0} \int_S e^{-i\mathbf{G}\cdot\mathbf{r}} ds - \frac{1}{\rho_0} \sum_{j=1}^{3} \int_{S_j^c} e^{-i\mathbf{G}\cdot\mathbf{r}} ds \right.$$
$$\left. + \left(\frac{1}{\rho_{CNT}} - \frac{1}{\rho_0}\right) \sum_{j=1}^{3} \int_{S_j^{CNT}} e^{-i\mathbf{G}\cdot\mathbf{r}} ds \right], \tag{7}$$

while the expression for $\epsilon(\mathbf{G})$ is obtained by replacing ρ with B in (7). The integration $\int_{S_j^c}$ is over the circular area of the cylinder with radius R_j, and $\int_{S_j^{CNT}}$ is over the area of its coating layer. Thus, Eq. (7)

leads to

$$
v(\mathbf{G}) = \begin{cases} \frac{1}{\rho_0} + \sum_{j=1}^{3}\left[\left(\frac{1}{\rho_{CNT}} - \frac{1}{\rho_0}\right)f_j^{CNT} - \frac{1}{\rho_{CNT}}f_j\right], & \mathbf{G} = \mathbf{0}, \\ \sum_{j=1}^{3}\left[\left(\frac{1}{\rho_{CNT}} - \frac{1}{\rho_0}\right)F_j^{CNT}(\mathbf{G}) - \frac{1}{\rho_{CNT}}F_j(\mathbf{G})\right]e^{-i\mathbf{G}\cdot\mathbf{r}_j^0}, & \mathbf{G} \neq \mathbf{0}. \end{cases} \tag{8}
$$

Equivalently, the expression for $\epsilon(\mathbf{G})$ can be derived. The structure factors are written as

$$
F_j(\mathbf{G}) = 2f_j\frac{J_1(|\mathbf{G}|R_j)}{|\mathbf{G}|R_j}, \tag{9}
$$

$$
F_j^{CNT}(\mathbf{G}) = 2f_j^{CNT}\frac{J_1(|\mathbf{G}|(R_j+I_j))}{|\mathbf{G}|(R_j+I_j)}. \tag{10}
$$

Supercell approximation

The rectangular supercell in Fig. 1c is composed of $N_c = 14$ unit cells of which $N_c/2$ cells comprise erected trimers and the other $N_c/2$ cells involve upside-down trimers. The area of each unit cell is $A_{uc} = a^2\sqrt{3}/2$. For this definition of the supercell, we choose the primitive lattice vectors $\mathbf{a}_1 = a\mathbf{x}$ and $\mathbf{a}_2 = (N_c a\sqrt{3}/2)\mathbf{y}$. Accordingly, the primitive reciprocal lattice vectors are $\mathbf{g}_1 = (2\pi/a)\mathbf{x}$ and $\mathbf{g}_2 = (4\pi/N_c a\sqrt{3})\mathbf{y}$, and $\mathbf{G} = \mathbf{G}_1 + \mathbf{G}_2$ with $\mathbf{G}_1 = n_1\mathbf{g}_1$ and $\mathbf{G}_2 = n_2\mathbf{g}_2$. According to the inner and outer radii of the coated cylinders, we consider the filling fractions $f = \pi R^2/A_{uc}$ and $f^{CNT} = \pi(R+I)^2/A_{uc}$. The position of the center of each cylinder contained at the n-th unit cell is denoted by the vector $\mathbf{r}_j^{(n)}$ with the origin at the center of the unit cell. Extending the integration in Eq. (4) over the whole supercell (of area $N_c A_{uc}$) the result can be expressed as

$$
v(\mathbf{G}) = \begin{cases} \frac{1}{\rho_0} + 3\left(\frac{1}{\rho_{CNT}} - \frac{1}{\rho_0}\right)f^{CNT} - \frac{1}{\rho_{CNT}}3f, & \mathbf{G} = \mathbf{0}, \\ \frac{1}{N_c}\sum_{n=1}^{N_c}e^{-i(n-1)G_2(a\sqrt{3}/2)}\left[\left(\frac{1}{\rho_{CNT}} - \frac{1}{\rho_0}\right)V_n(\mathbf{G}) - \frac{1}{\rho_{CNT}}W_n(\mathbf{G})\right], & \mathbf{G}\neq\mathbf{0}, \end{cases} \tag{11}
$$

with $G_2 = n_2|\mathbf{g}_2|$, and the extended structure factors

$$
W_n(\mathbf{G}) = \sum_{j=1}^{n_c} 2f_j\frac{J_1(|\mathbf{G}|R)}{|\mathbf{G}|R}e^{-i\mathbf{G}\cdot\mathbf{r}_j^{(n)}} \tag{12}
$$

$$
V_n(\mathbf{G}) = \sum_{j=1}^{n_c} 2f_j^{CNT}\frac{J_1(|\mathbf{G}|(R+I))}{|\mathbf{G}|(R+I)}e^{-i\mathbf{G}\cdot\mathbf{r}_j^{(n)}}, \tag{13}
$$

where n_c is the number of the cylinders in the n-th unit cell. As can be seen in Fig. 1c, here, we must account for units containing complete ($f_j = f$) and incomplete ($f_j = f/2$) trimers (same for the CNT coating).

Acoustic k · p theory

We adopt the $\mathbf{k}\cdot\mathbf{p}$ method in ref. [33] to derive the Hamiltonian around the K valley. We start from the case of $\beta = 0$. The Bloch functions around k_0 at the K point are expressed as linear combinations of the Dirac eigenstates,

$$
\psi_{l\mathbf{k}}(\mathbf{r}) = u_{l\mathbf{k}}(\mathbf{r})e^{i\mathbf{k}\cdot\mathbf{r}} = \sum_j A_{lj}(\mathbf{r})e^{i(\mathbf{k}-\mathbf{k}_0)\cdot\mathbf{r}}\psi_{j\mathbf{k}_0}(\mathbf{r}), \tag{14}
$$

where $\psi_{j\mathbf{k}_0}(\mathbf{r}) = u_{j\mathbf{k}_0}(\mathbf{r})e^{i\mathbf{k}_0\cdot\mathbf{r}}$ is the Bloch function at the Dirac point. The periodic function $u_{l\mathbf{k}}(\mathbf{r})$ is a linear combination of $u_{j\mathbf{k}_0}(\mathbf{r})$. By substituting this solution into the sound wave equation, we arrived at,

$$
\det\left|H - \frac{4\pi^2(f^2 - f_0^2)}{c^2}\right| = 0. \tag{15}
$$

where c is the velocity of sound, f is the frequency, and f_0 is the Dirac frequency. H is an effective Hamiltonian around the Dirac cone. Considering only the first order, the matrix element $H_{lj} = \Delta\mathbf{k}\cdot\mathbf{p}_{lj}$ with,

$$
\mathbf{p}_{lj} = \frac{4\pi^2}{\mathcal{A}}\int_{uc}\psi_{l\mathbf{k}_0}^*(\mathbf{r})\left[\frac{2i\nabla}{\rho(\mathbf{r})} + i\nabla\cdot\frac{1}{\rho(\mathbf{r})}\right]\psi_{j\mathbf{k}_0}(\mathbf{r})d\mathbf{r}. \tag{16}
$$

$\mathcal{A}$ is the area of a unit cell, $\rho(\mathbf{r})$ is relative density to air, and the orthogonality of the eigensolutions is given by $\frac{4\pi^2}{\mathcal{A}}\int_{uc}\psi_{l\mathbf{k}_0}^*(\mathbf{r})\frac{1}{B(\mathbf{r})}\psi_{j\mathbf{k}_0}(\mathbf{r})d\mathbf{r} = \delta_{lj}$ with $B(\mathbf{r})$ the relative bulk modulus. Next, we extend the point group symmetry to simplify the Hamiltonian. The system with a Dirac cone at the K point has the symmetry $C_{3v} = C_3 + 3\sigma_v$. Due to the invariance of a scalar product to symmetry operations, applying the symmetry operation $\widehat{R}$ to a wave vector $\mathbf{k}_0$, is equivalent to applying its inverse operator $\widehat{R}^{-1}$ to the physical space vector $\mathbf{r}$. The eigenstates at the K points after the operation of $\widehat{R}$ read,

$$
\widehat{P}_R\psi_{l\mathbf{k}_0}(\mathbf{r}) = \psi_{l\widehat{R}\mathbf{k}_0}(\mathbf{r}) = \psi_{l\mathbf{k}_0}(\widehat{R}^{-1}\mathbf{r}) = \sum_m D(\widehat{R})_{m,l}\psi_{m\mathbf{k}_0}(\mathbf{r}), \tag{17}
$$

where $D(\widehat{R})$ is an irreducible matrix representation. For $\widehat{R} = C_3$ or $\widehat{R} = \sigma_v$, we can chose,

$$
D(C_3) = \begin{pmatrix} -\frac{1}{2} & -\frac{\sqrt{3}}{2} \\ \frac{\sqrt{3}}{2} & -\frac{1}{2} \end{pmatrix}, \quad D(\sigma_v) = \sigma_z = \begin{pmatrix} 1 & 0 \\ 0 & -1 \end{pmatrix}. \tag{18}
$$

Based on Eq. (17), we can assume a new variable $\mathbf{r}' = \widehat{R}^{-1}\mathbf{r}$. Under this definition, wave functions undergo an operation $\widehat{R}^{-1}$ in the physical space, thus Eq. (16) becomes,

$$
\begin{aligned} \mathbf{p}_{lj} &= \frac{4\pi^2}{\mathcal{A}}\int_{uc}\psi_{l\mathbf{k}_0}^*(\mathbf{r}')\left[\frac{2i\nabla}{\rho(\mathbf{r}')} + i\nabla\cdot\frac{1}{\rho(\mathbf{r}')}\right]\psi_{j\mathbf{k}_0}(\mathbf{r}')d\mathbf{r}' \\ &= \widehat{R}^{-1}\sum_{m,n}D^*(\widehat{R})_{l,m}D(\widehat{R})_{n,j}\mathbf{p}_{mn}. \end{aligned} \tag{19}
$$

The relation of Eq. (19) links different matrix elements within the first-order correction. By applying $\widehat{R} = C_3$, the Hamiltonian can be simplified: $\mathbf{p}_{11} = -\mathbf{p}_{22}$, $\mathbf{p}_{12} = \mathbf{p}_{21}$, $\mathbf{p}_{12} = i\sigma_y\mathbf{p}_{11}$. Similarly, applying $\widehat{R} = \sigma_v$, we obtain $\mathbf{p}_{11y} = -\mathbf{p}_{22y} = 0$, $\mathbf{p}_{12x} = \mathbf{p}_{21x} = 0$. Thus, the Hamiltonian reads $H = |\mathbf{p}_{11}|(\Delta k_x\sigma_z - \Delta k_y\sigma_x)$. By a unitary transformation using $U = [1, i; 1, -i]$, H is mapped to a Dirac Hamiltonian,

$$
\Delta\mathcal{H}_D = v_D(\Delta k_x\sigma_x + \Delta k_y\sigma_y). \tag{20}
$$

v_D is the Dirac velocity. If the trimers are rotated by $\pi/6$, the mirror symmetry σ_v is broken and the Dirac cone is lifted. The Hamiltonian around the K valley becomes

$$
\Delta\mathcal{H}\psi = (\Delta\mathcal{H}_D + a_0'\sigma_0 + b_0'\sigma_z)\psi = (f - f_0)\psi, \tag{21}
$$

where $a_0' = a_0 + i\gamma_0$, $b_0' = b_0 + i\gamma_1$. More specifically, $\Delta\mathcal{H}$ takes to form

$$
\Delta\mathcal{H} = \begin{bmatrix} (a_0 + i\gamma_0) + (b_0 + i\gamma_1) & v_D(\Delta k_x - i\Delta k_y) \\ v_D(\Delta k_x + i\Delta k_y) & (a_0 + i\gamma_0) - (b_0 + i\gamma_1) \end{bmatrix}. \tag{22}
$$

Above, b_0 is an effective mass that breaks the Dirac cone. a_0 is a bias to slightly shift the frequency due to the perturbation (rotating the trimers to open the Dirac cone). γ_0, γ_1 originate from the non-Hermitian (gain) contribution. Using finite element simulation data, the coefficients are fitted to the values given in Table 1. Equation (21) leads to the following dispersion relation

$$
f_{\pm} = f_0 + a_0 + i\gamma_0 \pm \sqrt{v_D^2(\Delta k_x^2 + \Delta k_y^2) + (b_0 + i\gamma_1)^2}. \tag{23}
$$

Table 1.	Coefficients of the Hamiltonian.				
β	v_D	a_0	b_0	γ_0	γ_1
0.05	29.72	45.95 Hz	525.25 Hz	−21.21 Hz	6.21 Hz

At the K point, $\Delta k_x = \Delta k_y = 0$, thus, the two eigenfrequencies are

$$f_\pm = f_0 + a_0 + i\gamma_0 \pm (b_0 + i\gamma_1). \tag{24}$$

Therefore, $f_+ = 9316.2 - 15i$ Hz and $f_- = 8265.7 - 27.42i$ Hz. If one considers $\gamma_1 \ll b_0$ namely $b_0' \approx b_0$, it leads to

$$f_\pm \approx f_0 + a_0 + i\gamma_0 \pm \sqrt{v_D^2(\Delta k_x^2 + \Delta k_y^2) + b_0^2}. \tag{25}$$

From here, it can be seen that the system, in the presence of (marginal) acoustic gain, remains quasi-Hermitian since only the eigenfrequency will be affected by it.

Multiple scattering theory

If an external pressure field P^0 (e.g., the field of point sources) impinges the 2D arrangement of N-cylinders represented in Fig. 2c, the total scattered field by all the individual constituent cylinder is given by Eq. (2) where $(A_a)_q$ are the coefficients to be determined. To this end, we focus on the total field incident on the a-cylinder which can be expanded in terms of Bessel functions J_q (of order q) as follows

$$P_a^0(r_a, \theta_a) = \sum_{q=-\infty}^{\infty} (B_a)_q J_q(k_0 r_a) e^{iq\theta_a}, \tag{26}$$

whose coefficients are related with $(A_a)_q$ by means of the transfer matrix T of the a-cylinder; $(A_a)_q = \sum_s (T_a)_{qs}(B_a)_s$. In the case of fluid cylinders of circular cross section with radius R, the matrix T is diagonal, i.e., $(T_a)_{qs} = (T_a)_q \delta_{qs}$. Since the triangular WG under study (Fig. 2c) is made of identical cylinders, we eliminate the subscript a from the notation of the matrix elements

$$T_q = -\frac{\rho_q J_q'(k_0 R) - J_q(k_0 R)}{\rho_q H_q'(k_0 R) - H_q(k_0 R)}, \quad \rho_q = \frac{\rho_c c_c}{\rho_0 c_0} \frac{J_q(k_c R)}{J_q'(k_c R)}, \tag{27}$$

where $k_c = \omega/c_c$, and the prime $(')$ implies derivative of the corresponding function with respect to the argument. For our present case regarding rigid cylinders, $\rho_c \to \infty$, Eq. (27) simplifies to $T_q = -J_q'(k_0 R)/H_q'(k_0 R)$. The total field is the sum of the external field P^0 and the field scattered by all the cylinders except a, $P_{\beta \neq a}^{sc}$. These two fields can be expressed in the reference frame of the a-cylinder by means of the Graft's addition theorem

$$P^0 = \sum_{q=-\infty}^{\infty} (A_a^0)_q J_q(k_0 r_a) e^{iq\theta_a}, \tag{28}$$

and from Eq. (2)

$$P_{\beta \neq a}^{sc} = \sum_{s=-\infty}^{\infty} \sum_{q=-\infty}^{\infty} \sum_{\beta \neq a} (A_\beta)_s H_{q-s}(k_0 r_{a\beta}) e^{i(s-q)\theta_{a\beta}} J_q(k_0 r_a) e^{iq\theta_a}. \tag{29}$$

The amplitudes $(A_a^0)_q$ of the incident field are assumed to be known. Thus, by truncating the indexes in Eqs. (26), (28), and (29) to some maximum value m and reformulating the equation $P_a^0(r_a, \theta_a) = P^0 + P_{\beta \neq a}^{sc}$ into matrix form, we obtain a systems of $N(2m + 1)$ linear equations for the unknown scattered amplitudes $(A_a)_q$. An acoustic point source of order s located at $\mathbf{R}_0$ is defined by a Hankel function of the same order by means of the pressure field $P_s(\mathbf{r}) = C_s H_s(k_0 r_s) e^{is\theta_s}$, where (r_s, θ_s) are the polar coordinates that represent the position vector $\mathbf{r}_s$ in the reference frame of the source $(\mathbf{r}_s = \mathbf{r} - \mathbf{R}_0)$ and C_s is a complex constant. Therefore, in the reference frame of the a-cylinder, the external field of N_s point sources of order s located at $\mathbf{R}_j$ (with $j = 1, 2, \ldots, N_s$) can be expressed as (28) with

$$(A_a^0)_q = \sum_{j=1}^{N_s} C_s H_{q-s}(k_0 r_{aj}) e^{i(s-q)\theta_{aj}}, \tag{30}$$

being $\mathbf{r}_{aj} = (r_{aj}, \theta_{aj})$ the position vector of the j-th point source in the reference frame of the a-cylinder located at $\mathbf{R}_a$, i.e., $\mathbf{r}_{aj} = \mathbf{R}_j -$

$\mathbf{R}_a$. Each source-ring used to model the active rods comprises n_p monopole point sources $(s = 0)$ that emit sound at the same phase. Consequently, Eq. (30) is computed for $N_s = n_p \times$ number of active rods. To control the relative phase among the source-rings within the unit cell, we replace the constant C_s by $C_s e^{i\psi_j}$ in Eq. (30), where the phase ψ_j takes one of the values $\phi_1 = 0$, $\phi_2 = 2\pi/3$ or $\phi_3 = -2\pi/3$ according to the arrangement indicated in the inset of Fig. 2a. In this way, we are able to set the appropriate gain-phase texture that breaks the chiral symmetry of the WG modes.

REFERENCES
1. Rycerz, A., Tworzydło, J. & Beenakker, C. Valley filter and valley valve in graphene. *Nat. Phys.* **3**, 172–175 (2007).
2. Xiao, D., Yao, W. & Niu, Q. Valley-contrasting physics in graphene: magnetic moment and topological transport. *Phys. Rev. Lett.* **99**, 236809 (2007).
3. Zhang, F., MacDonald, A. H. & Mele, E. J. Valley Chern numbers and boundary modes in gapped bilayer graphene. *Proc. Natl Acad. Sci. USA* **110**, 10546–10551 (2013).
4. Ma, T. & Shvets, G. All-Si valley-Hall photonic topological insulator. *New J. Phys.* **18**, 025012 (2016).
5. Dong, J.-W., Chen, X.-D., Zhu, H., Wang, Y. & Zhang, X. Valley photonic crystals for control of spin and topology. *Nat. Mater.* **16**, 298–302 (2017).
6. Noh, J., Huang, S., Chen, K. P. & Rechtsman, M. C. Observation of photonic topological valley Hall edge states. *Phys. Rev. Lett.* **120**, 063902 (2018).
7. Gao, F. et al. Topologically protected refraction of robust kink states in valley photonic crystals. *Nat. Phys.* **14**, 140–144 (2018).
8. Orazbayev, B. & Fleury, R. Quantitative robustness analysis of topological edge modes in C6 and valley-Hall metamaterial waveguides. *Nanophotonics* **8**, 1433–1441 (2019).
9. Zhang, Z. et al. Topological acoustic delay line. *Phys. Rev. Appl.* **9**, 034032 (2018).
10. Miniaci, M., Pal, R. K., Manna, R. & Ruzzene, M. Valley-based splitting of topologically protected helical waves in elastic plates. *Phys. Rev. B* **100**, 024304 (2019).
11. Xiong, W. et al. Demultiplexing sound in stacked valley-Hall topological insulators. *Phys. Rev. B* **104**, 224108 (2021).
12. Lee, T. E. Anomalous edge state in a non-Hermitian lattice. *Phys. Rev. Lett.* **116**, 133903 (2016).
13. Gong, Z. et al. Topological phases of non-Hermitian systems. *Phys. Rev. X* **8**, 031079 (2018).
14. Kunst, F. K., Edvardsson, E., Budich, J. C. & Bergholtz, E. J. Biorthogonal bulk-boundary correspondence in non-Hermitian systems. *Phys. Rev. Lett.* **121**, 026808 (2018).
15. Longhi, S. Topological phase transition in non-Hermitian quasicrystals. *Phys. Rev. Lett.* **122**, 237601 (2019).
16. Zhang, Z., Rosendo López, M., Cheng, Y., Liu, X. & Christensen, J. Non-Hermitian sonic second-order topological insulator. *Phys. Rev. Lett.* **122**, 195501 (2019).
17. Zhao, H. et al. Non-Hermitian topological light steering. *Science* **365**, 1163–1166 (2019).
18. Xue, H., Wang, Q., Zhang, B. & Chong, Y. D. Non-Hermitian Dirac Cones. *Phys. Rev. Lett.* **124**, 236403 (2020).
19. Brandenbourger, M., Locsin, X., Lerner, E. & Coulais, C. Non-reciprocal robotic metamaterials. *Nat. Commun.* **10**, 1–8 (2019).
20. Ghatak, A., Brandenbourger, M., van Wezel, J. & Coulais, C. Observation of non-Hermitian topology and its bulk-edge correspondence in an active mechanical metamaterial. *Proc. Natl Acad. Sci. USA* **117**, 29561–29568 (2020).
21. Zhu, X. et al. Photonic non-Hermitian skin effect and non-Bloch bulk-boundary correspondence. *Phys. Rev. Res.* **2**, 013280 (2020).
22. Yao, S. & Wang, Z. Edge states and topological invariants of non-Hermitian systems. *Phys. Rev. Lett.* **121**, 086803 (2018).

23. Song, F., Yao, S. & Wang, Z. Non-Hermitian topological invariants in real space. *Phys. Rev. Lett.* **123**, 246801 (2019).

24. Okuma, N., Kawabata, K., Shiozaki, K. & Sato, M. Topological origin of non-Hermitian skin effects. *Phys. Rev. Lett.* **124**, 086801 (2020).

25. Xiao, L. et al. Non-Hermitian bulk-boundary correspondence in quantum dynamics. *Nat. Phys.* **16**, 761–766 (2020).

26. Helbig, T. et al. Generalized bulk–boundary correspondence in non-Hermitian topolectrical circuits. *Nat. Phys.* **16**, 747–750 (2020).

27. Weidemann, S. et al. Topological funneling of light. *Science* **368**, 311–314 (2020).

28. Gao, P., Willatzen, M. & Christensen, J. Anomalous topological edge states in non-Hermitian piezophononic media. *Phys. Rev. Lett.* **125**, 206402 (2020).

29. Yi, Y. & Yang, Z. Non-Hermitian skin modes induced by on-site dissipations and chiral tunneling effect. *Phys. Rev. Lett.* **125**, 186802 (2020).

30. Shankar, S. et al. Topological active matter. *Nat. Rev. Phys.* **4**, 380–398 (2022).

31. Zhang, X., Zhand, T., Lu, M.-H. & Chen, Y.-F. A review on non-Hermitian skin effect. *Adv. Phys-X* **7**, 2109431 (2022).

32. Hu, B. et al. Non-Hermitian topological whispering gallery. *Nature* **597**, 655–659 (2021).

33. Mei, J., Wu, Y., Chan, C. T. & Zhang, Z.-Q. First-principles study of Dirac and Dirac-like cones in phononic and photonic crystals. *Phys. Rev. B* **86**, 035141 (2012).

34. Zhang, Z. et al. Directional acoustic antennas based on valley-hall topological insulators. *Adv. Mater.* **30**, 1803229 (2018).

AUTHOR CONTRIBUTIONS

R.P.S. conducted the PWE and MST simulations. L.Y.Z. derived the k · p theory. Z.Z. and P.G. assisted in the numerical developments. Y.C. and J.C. conceived the project. R.P.S. and J.C. wrote the paper.

COMPETING INTERESTS

The authors declare no competing interests.

ADDITIONAL INFORMATION

Correspondence and requests for materials should be addressed to René. Pernas-Salomón, Ying Cheng or Johan Christensen.

Reprints and permission information is available at http://www.nature.com/reprints

Publisher's note Springer Nature remains neutral with regard to jurisdictional claims in published maps and institutional affiliations.